RESEARCH ARTICLE | JULY 09 2025

Numerical and experimental investigation of three-electrode air discharge: Propagation characteristics and optimization strategies

Bo Yin; Xiaochi Ma; Yifei Zhu; Yun Wu; Borui Zheng

Phys. Plasmas 32, 073505 (2025)
https://doi.org/10.1063/5.0261134

Physics of Plasmas ARTICLE pubs.aip.org/aip/pop

Numerical and experimental investigation of three-electrode air discharge: Propagation characteristics and optimization strategies

Cite as: Phys. Plasmas **32**, 073505 (2025); doi: 10.1063/5.0261134
Submitted: 29 January 2025 · Accepted: 24 June 2025 ·
Published Online: 9 July 2025

Bo Yin,[1] Xiaochi Ma,[1] Yifei Zhu,[1,a)] Yun Wu,[1,b)] and Borui Zheng[2]

AFFILIATIONS

[1]National Key Lab of Aerospace Power System and Plasma Technology, Xi'an Jiaotong University, Xi'an 710038, People's Republic of China
[2]School of Automation and Information Engineering, Xi'an University of Technology, Xi'an 710048, People's Republic of China

[a)]Author to whom correspondence should be addressed: yifei.zhu.plasma@gmail.com
[b)]Electronic mail: wuyun1223@126.com

ABSTRACT

Low-temperature plasma technology has demonstrated significant potential for applications such as gas treatment and energy conversion. This study investigates the optimization of a three-electrode discharge system, combining dielectric barrier discharge (DBD) and direct current (DC) discharge at ambient conditions. By experiment and simulation, the effects of electrode geometry, location, and discharge parameters on plasma stability are analyzed. Results reveal that DC-induced pre-ionization plays a crucial role in transitioning from streamer to diffuse discharge, requiring a minimum pre-ionization density of 2×10^{17} m^{-3}. Smaller electrode diameters enhance the electric field and reactive species densities, while optimized discharge gaps ensure stable and spatial discharge. A minimum voltage of -6 kV (DC) and 3.5 kV (DBD) are necessary for breakdown, with breakdown time decreasing as voltage increases. Power analysis shows dominant energy consumption by the DBD component, emphasizing the need for DBD voltage minimization to improve energy efficiency. These findings provide valuable insights into achieving stable and energy-efficient plasma discharges, offering a foundation for scalable applications in gas treatment and related fields.

I. INTRODUCTION

Low-temperature plasma technology has demonstrated significant potential in air pollutant degradation and energy conversion. The plasma contains abundant reactive species (electrons, excited state particles, ions and free radicals) to oxidize and decompose gas molecules. Compared with traditional treatment methods (thermal cracking, catalytic oxidation, adsorption, etc.), plasma technology has the advantages of high efficiency and low energy consumption, high product selectivity, simple operation and stable operation. Currently, various plasma discharge methods have been explored for gas treatment, including dielectric barrier discharge,[1] gliding arc discharge,[2] corona discharge,[3] spark discharge,[4] nanosecond pulse discharge,[5] and microwave discharge.[6] Among these, dielectric barrier discharge (DBD) is widely adopted in engineering applications due to its ability to prevent transition into spark or arc discharges. However, DBD still faces challenges such as filamentary discharge and high wind resistance. Filamentary discharges exhibit high energy density and elevated gas temperatures, which can potentially damage heat-sensitive materials. In contrast, diffuse discharges possess lower energy and gas temperatures, representing an intermediate state between corona and spark discharges. A characteristic of diffuse discharge is volumetric nature, featuring divergent and non-constricted plasma channels. Achieving diffuse discharge in atmospheric pressure air is challenging, and non-equilibrium plasma can easily transition into local thermodynamic equilibrium plasma. To address this, researchers commonly utilize two methods for achieving diffuse discharge: (1) using a nanosecond pulse source to shorten the discharge time below that of thermal arc discharges and (2) optimizing the electrode structure to stabilize the discharge.

Soloviev[7] studied the surface dielectric barrier discharge in atmospheric pressure air by the simulation and experiment. They found that the discharge corresponding to the trailing edge is not diffuse and demonstrates a well-pronounced streamer-like shape. Tao Shao[8] investigated the nanosecond pulsed DBD discharge at atmospheric pressure, captured the discharge images with a low-speed camera to observe the glow discharge and filamentary discharge. They found that the discharge gap, dielectric type, and the discharge frequency are the important factors affecting the transition of the two discharge modes. Fridman[9] analyzed the uniformity of DBD by ICCD, and the results showed that the uniformity of DBD depends on the electric field, with less impact from the rising time of the high-voltage pulse. Zeyu Hao[9] investigated the effects of different dielectric thicknesses and materials, electrode types, and applied voltages on DBD discharge, finding that mica dielectrics and stainless-steel blade electrodes enhanced discharge uniformity. Belinger *et al.*[10] used a new experimental method to study the effect of dielectric thickness on the uniformity of DBD discharge by controlling the current density, achieving a diffuse discharge at 5 kHz for the first time.

As plasma research advances, emerging scientific challenges in plasma treatment require further investigation, including (1) enhancing the stability and efficiency of plasma sources and (2) exploring the mechanisms behind the generation of active species. The development of stable, efficient plasma sources that ensure uniformity over large areas and effectiveness in complex engineering environments is crucial. The generation and role of active species such as electrons, ions, excited state particles, and free radicals are central to addressing gas treatment challenges. While nanosecond pulse excitation demonstrates superior chemical activity, its practical implementation faces limitations such as electromagnetic interference and system instability. Furthermore, conventional electrode configurations exhibit inherent limitations in both spatial controllability and aerodynamic performance. To overcome these limitations, we developed a novel three-electrode discharge configuration with optimized structural parameters to achieve stable plasma generation. The discharge characteristics were systematically investigated through a combined approach of numerical simulations and experimental measurements, with particular focus on evaluating how electrode geometry and operational parameters influence discharge stability and intensity.

This work presents a methodology for building a two-dimensional fluid model, which is compared with experimental data to comprehensively analyze the propagation mechanisms. The framework, a description of the model and the implementation of experimental conditions are given in Sec. II, results and discussions are presented in Sec. III, and the conclusions are drawn in Sec. IV.

II. EXPERIMENTAL SETUP AND MODEL DESCRIPTION

A. Implementation of experimental conditions

Figure 1 presents the schematic of the three-electrode discharge system operating under ambient conditions, which integrates two discharge components: a dielectric barrier discharge (DBD) and a direct current (DC) discharge. The medium of DBD is made of alumina ceramic with a thickness of 1 mm, a width of 10 mm, and a length of 150 mm. The electrodes are made from stainless steel with a thickness of 1 mm and a width of 3 mm. DBD is driven by a nanosecond pulsed generator (FID power supply: FPG 50-50NX2). The DC electrode is made of tungsten needle with a diameter of 0.5–1 mm and a length of 150 mm, driven by negative high voltage power supply. The inter-electrode distance ($d = 7$–10 mm) defines the primary plasma generation region. For the gas treatment experiments, the plasma generation system is integrated within a sealed chamber designed to precisely control the gas treatment volume. The experimental system incorporates precision-calibrated mass flow controller to quantitatively monitor all input gas. This closed-loop design ensures reliable measurement of key treatment parameters, including decomposition efficiency and by-product formation, while maintaining well-controlled environmental conditions.

Voltage and current are the critical parameters for characterizing the pulse discharge and mode conversion. A voltage probe (North Star PVM-5, 0–60 kV/90 MHz) and a current probe (CWT15B, 3 kA/50 MHz) are utilized to monitor the applied voltage and current. These probes are linked with a digital oscilloscope (Tek MDO34, 100 MHz–1 GHz, 3 kA/50 MHz) to capture and analyze crucial electrical parameters. An intensified charge coupled device (ICCD) high-speed camera (Andor iStar DH334T) is used to capture the temporal and spatial evolution of plasma, which is capable of capturing low-light images with exposure times as fast as 2 ns. The nanosecond power supply and the camera are triggered by a signal generator to synchronize the initial discharge with the camera, capturing the spatial-temporal evolution of different plasma phases by adjusting the camera delay.

B. The description of the fluid model

The fundamental physical mechanism of the gas discharge is difficult to obtain by experiment. Therefore, a plasma fluid model (PASSKEy) is used to calculate spatial-temporal evolution of the electric field, species densities, and fluid dynamics. Zhu *et al.*[11] used a numerical model and existing experimental data to analyze the mechanisms and energy characteristics of the nSDBD-based plasma-assisted anti-icing. Zhu and Starikovskaia[12] used a numerical model to study the effect of heat release in reactions with charged and electronically excited species. Ma *et al.*[13] used a numerical model to analyze the pre-ionization process and its influence on the breakdown characteristics in the operation of ArF excimer lasers. However, this paper used a numerical model to investigate the optimization of a three-electrode discharge system, combining DBD and DC discharge. Detailed mathematical methods and model validations can be found in previous publications.[13] In this section, we briefly describe the equations solved in model for this investigation.

1. Governing equations

PASSKEy adopts a comprehensive computational framework that self-consistently solves the coupled system of governing equations for non-equilibrium plasma dynamics. The numerical scheme simultaneously resolves the Poisson equation for electric potential distribution, drift-diffusion equations for charged species transport, and the electron energy equation for mean energy characterization, while additionally incorporating Helmholtz equations to account for photoionization effects. The Poisson equation is used to calculate the electric field of the whole computational domain as follows:

$$\nabla(\varepsilon_0\varepsilon_r\nabla\Phi) = -\rho - \rho_c\delta_s, \tag{1}$$

$$E = -\nabla\Phi, \quad \rho = \sum\nolimits_{i=1}^{N_{\mathrm{ch}}} q_i n_i, \tag{2}$$

where ε_0 and ε_r are the permittivity and relative permittivity, respectively, Φ is the electric potential, E is the electric field, ρ_c is the dielectric surface charge, δ_s is the Kronecker equation, q_i and n_i are density and charge of species i, respectively, N_{ch} is a number of the charged species.

The drift-diffusion equations based on local field approximation are given by

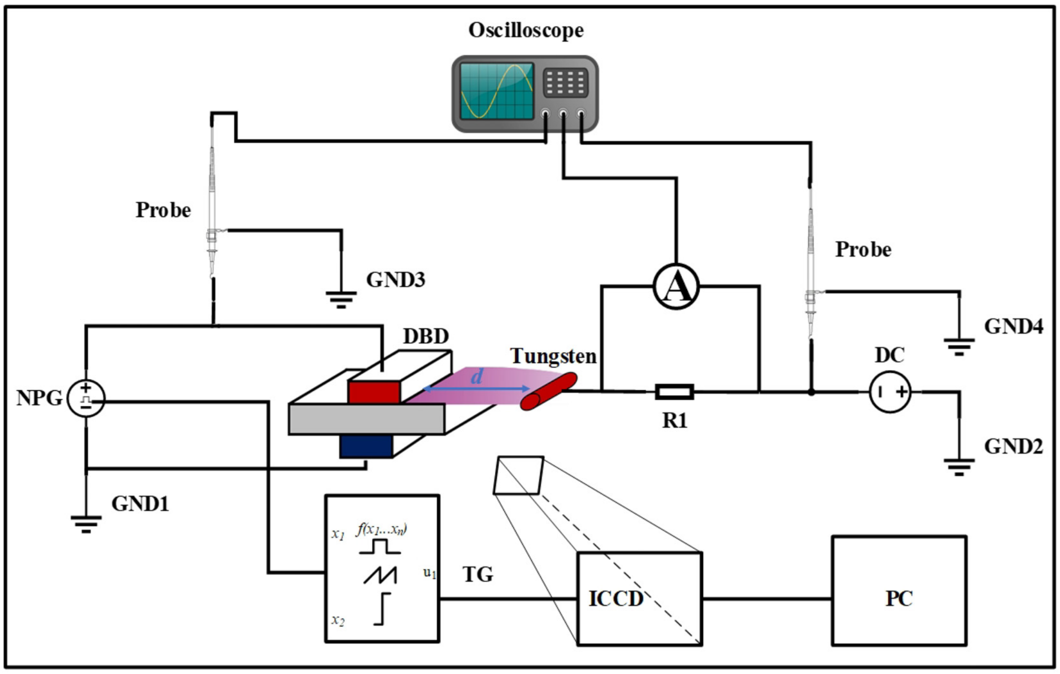

FIG. 1. A brief description of the experimental setup for three-electrode discharge. DC is a direct current generator. NPG is a nanosecond pulse generator, TG is a triggering generator, Probe is a high voltage probe, ICCD is an intensified charge coupled device, PC is a personal computer. *d* is the distance between DBD and direct current electrode, and R1 is 1 kΩ. The symbol A denotes a differential voltage probe connected across a 1 kΩ precision resistor to measure discharge current.

$$\frac{\partial n_i}{\partial t} + \nabla \cdot \boldsymbol{\Gamma}_i = S_i + S_{\mathrm{ph}}, \quad i = 1, 2, \ldots, N_{\mathrm{total}}, \tag{3}$$

$$\boldsymbol{\Gamma}_i = (q_i/|q_i|)\mu_i n_i E - D_i \nabla n_i, \quad i = 1, 2, \ldots, N_{\mathrm{ch}}, \tag{4}$$

where $\boldsymbol{\Gamma}_i$ and n_i are the species flux and the number of density of $i_t h$ species, respectively; S_i and S_{ph} are reaction source and photoionization source, respectively;q_i, μ_i, and D_i are the charge, mobility, and diffusion coefficient, respectively. The electron transport coefficients (μ_e and D_e) and electron collision reaction rate coefficients can be obtained using BOLSIG+.[14] The ion transport coefficients can be found in Ref. 15 or using the MOBION software package. The photoionization source is used to calculate photoionization for the mixture of nitrogen and oxygen by the Helmholtz model, whose fitting parameters are given by the measured photo function.

Typically, the Local Mean Energy Approximation (LMEA) and Local Field Approximation (LFA) are commonly employed in the numerical simulation of plasma. The robustness of LFA has been extensively discussed in Ref. 16. However, in the near-wall region, where the lower side of the plasma is close to the dielectric surface, the LFA ignores a strong electron density gradient region in the sheath, leading to an overestimation of ionization.[17] Conversely, the LMEA demonstrates greater accuracy, particularly in modeling positive streamers and plasma interactions with dielectrics.[18] Therefore, to achieve more precise simulation in the three-electrode discharge, we have adopted the LMEA in our numerical model. The drift-diffusion equations for the mean electron energy are shown in the following equations:

$$\frac{\partial}{\partial t}(n_{\mathrm{em}}) + \nabla \cdot \boldsymbol{\Gamma}_\epsilon = -|q_{\mathrm{e}}| \boldsymbol{\Gamma}_{\mathbf{e}} \cdot \mathbf{E} - P(\epsilon_{\mathrm{m}}), \tag{5}$$

$$\boldsymbol{\Gamma}_\epsilon = -\mu_\epsilon n_{\mathrm{e}} \epsilon_{\mathrm{m}} \mathbf{E} - D_\epsilon \nabla (n_{\mathrm{e}} \epsilon_{\mathrm{m}}), \tag{6}$$

where $\boldsymbol{\Gamma}_e$ and n_e are the electron energy flux and the electron density, respectively; q_e, μ_ϵ, and D_ϵ are the electron charge, mobility, and diffusion coefficient of electron energy, respectively, n_e, $\boldsymbol{\Gamma}_\epsilon$, and q_e are the electron density, electron energy flux, and electron charge, respectively; E, ϵ_m, and $P(\epsilon_m)$ are the electric field, mean electron energy, and the power lost by electron collisions, respectively.

2. Reaction kinetic scheme

A suitable reaction kinetic scheme is crucial for revealing the physical mechanisms. In the present work, a reduced reaction kinetic scheme for decreasing computational time is selected based on the published work,[12] including ionization, excitation, attachment, charge transfer, and recombination processes. The following neutral, charged, and excited species are taken into account: $\mathrm{e}, \mathrm{N}_2, \mathrm{N}_2(\mathrm{A}^3\ \Sigma_u^+), \mathrm{N}_2(\mathrm{B}^3\ \Pi_{\mathrm{g}}, \mathrm{N}_2(\mathrm{C}^3\Pi_{\mathrm{u}}), \mathrm{N}_2^+\mathrm{N}_4^+, \mathrm{O}_2, \mathrm{O}, \mathrm{O}(^1\mathrm{D}), \mathrm{O}_2^+, \mathrm{O}_4^+, \mathrm{O}^-, \mathrm{O}_2^-, \mathrm{O}_2^+\mathrm{N}_2$. Detailed reactions and corresponding rates are given in Table I. The rate constant unit of single-body reaction is s^{-1}, the rate constant unit of two-body reaction is cm^3/s, and the rate constant unit of three-body reaction is cm^6/s. Te is taken as a function of mean electron energy based on BOLSIG+ with cross section. Tgas is calculated using the fluid module in PASSKEy.

This simplification is based on a sensitivity analysis that identified the most critical reactions influencing the key physical and chemical

TABLE I. Reduced kinetics scheme of air. Rate constants are given in s^{-1}, m^3/s, and m^6/s, T_{gas} (gas temperature) and T_e (electron temperature) are given in K.

No.	Reaction	Rate constant	Ref.
R1	$e+N_2 \rightarrow e+e+N_2^+$	$f(\sigma, \epsilon_m)$	19
R2	$e+O_2 \rightarrow e+e+O_2^+$	$f(\sigma, \epsilon_m)$	20
R3	$e+O_2 \rightarrow O^-+O$	$f(\sigma, \epsilon_m)$	19
R4	$e+N_2 \rightarrow e+N_2(A^3\Sigma_u^+)$	$f(\sigma, \epsilon_m)$	19
R5	$e+N_2 \rightarrow e+N_2(B^3\Pi_g)$	$f(\sigma, \epsilon_m)$	19
R6	$e+N_2 \rightarrow e+N_2(C^3\Pi_u)$	$f(\sigma, \epsilon_m)$	19
R7	$e+O_2 \rightarrow e+O+O$	$f(\sigma, \epsilon_m)$	21
R8	$e+O_2 \rightarrow e+O+O(^1D)$	$f(\sigma, \epsilon_m)$	21
R9	$N_2^++N_2+N_2 \rightarrow N_4^++N_2$	5×10^{-29}	22
R10	$N_2^++N_2+O_2 \rightarrow N_4^++O_2$	5×10^{-29}	21
R11	$N_4^++O_2 \rightarrow O_2^++N_2+N_2$	2.5×10^{-10}	23
R12	$N_2^++O_2 \rightarrow O_2^++N_2$	6×10^{-11}	23
R13	$O_2^++N_2+N_2 \rightarrow O_2^++N_2+N_2$	9×10^{-31}	23
R14	$O_2^++N_2+O_2 \rightarrow O_2^++N_2+O_2$	9×10^{-31}	23
R15	$O_2^++N_2 \rightarrow O_2^++N_2$	4.3×10^{-10}	23
R16	$O_2^++O_2 \rightarrow O_2^++N_2$	10^{-9}	23
R17	$O_2^++O_2 \rightarrow O_4^++O_2$	2.4×10^{-30}	23
R18	$e+O_2+O_2 \rightarrow O_2^++O_2$	$2 \times 10^{-29}(300/T_e)$	23
R19	$O^-+O^+ \rightarrow e+O_2$	1.4×10^{-10}	24
R20	$O_2^++O \rightarrow e+O_2+O$	1.5×10^{-10}	24
R21	$e+N_4^++N_2 \rightarrow N_4+N_2(C^3\Pi_u)$	$2.3 \times 10^{-6}(300/T_e)^{0.5}$	24
R22	$e+N_2^+ \rightarrow N+N$	$1.8 \times 10^{-7}(300/T_e)^{0.39}$	24
R23	$e+O_4^+ \rightarrow O+O_2$	$1.4 \times 10^{-6}(300/T_e)^{0.50}$	24
R24	$e+O_2^+ \rightarrow O+O_2$	$2.0 \times 10^{-7}(300/T_e)$	24
R25	$O_2^++O_2 \rightarrow O^++O_2+N_2$	10^{-7}	23
R26	$O_2^++O_4^++O_2+O_2 \rightarrow O_2^++O_2$	2.0×10^{-25}	23
R27	$O_2^++O_2^++O_2 \rightarrow O_2+O_2+O_2+O_2$	2.0×10^{-25}	23
R28	$O_2^++O_2^++N_2 \rightarrow O_2+O_2+N_2$	2.0×10^{-25}	23
R29	$O_2^++O_2+O_2 \rightarrow O_2+O_2+O_2$	2.0×10^{-25}	23
R30	$O^-+N_2^+ \rightarrow O+N+N$	$2.0 \times 10^{-7}(300/T_e)$	21
R31	$N_2(C^3\Pi_u)+N_2 \rightarrow N_2(B^3\Pi_g)+N_2$	1.0×10^{-11}	21
R32	$N_2(C^3\Pi_u)+O_2 \rightarrow N_2+O+O(^1D)$	3.0×10^{-10}	21
R33	$N_2(C^3\Pi_u) \rightarrow N_2+h\nu$	2.45×10^{-7}	21
R34	$N_2(B^3\Pi_g)+O_2 \rightarrow N_2+O+O$	3.0×10^{-10}	21
R35	$N_2(B^3\Pi_g)+N_2 \rightarrow N_2(A^3\Sigma_u^+)+N_2(v)$	1.0×10^{-11}	21
R36	$N_2(A^3\Sigma_u^+)+O_2 \rightarrow N_2+O+O$	$2.5 \times 10^{-12}(T_{gas}/300)^{0.5}$	21
R37	$O(^1D)+O_2 \rightarrow O+O_2$	$3.3 \times 10^{-11}(67/T_{gas})$	21
R38	$O(^1D)+N_2 \rightarrow O+N_2$	$1.8 \times 10^{-11}(107/T_{gas})$	21

processes under our specific conditions. By focusing on these 38 reactions, we achieve a balance between computational efficiency and the accuracy of our results. Figure 2 shows a comparison of the calculated species densities between the full kinetic scheme and the simplified kinetic scheme. The KIN2 kinetic scheme demonstrates good agreement with the full kinetic scheme in terms of the calculated temporal behavior of the densities and emissions.

3. Computational domain and boundary conditions

The simplified geometry used for the calculation is shown in Fig. 3 with the high voltage electrode in yellow, the medium in cyan, the ground in green, the DC bias electrode in red, and the plasma calculation region in blue. A computational domain of size 50 × 50 mm is assigned. We use the structured adaptive mesh refinement (SAMR)

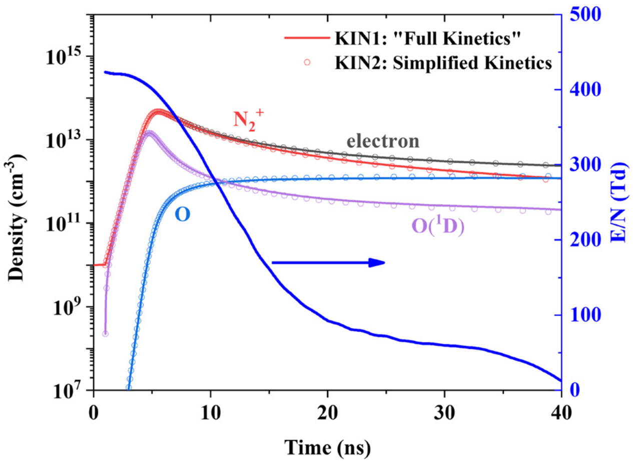

FIG. 2. Comparison of the calculated species densities between the full kinetic scheme "KIN1" and the simplified kinetic scheme "KIN2."

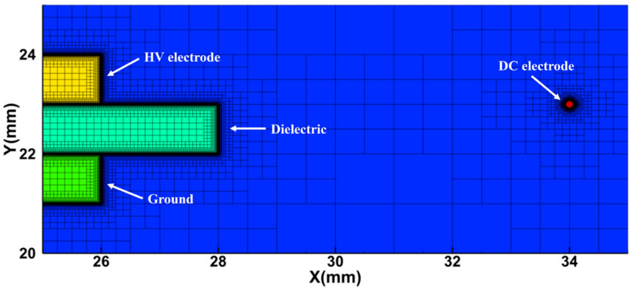

FIG. 3. 2D geometry for three-electrode discharge with structured adaptive mesh refinement, with the high voltage electrode in yellow, the medium in cyan, the ground in green, the DC electrode in red, and the plasma calculation region in blue.

in a 2D Cartesian coordinate system to initialize grids. The reduced computational domain and refined mesh distribution are shown in Fig. 3. The criteria of adaptive mesh refinement based on the electron density are expressed as follows:

$$h = h_{\max}\frac{1}{2^n} \le \max\left\{\frac{18 - \log_{10}(n_e)}{\log_{10}(n_e)}h_{\max} + \frac{18}{\log_{10}(n_e)}h_{\min}, h_{\min}\right\}, \tag{7}$$

where h, h_{min}, h_{max} are the mesh size, the minimal mesh size, and the maximum mesh size, respectively; n_e and n are the electron density and the number of refinement times, respectively. To be able to resolve the fine discharge structure, the computational mesh should be not greater than 2 μm for atmospheric pressure air.[25] In a result, we set the minimal mesh size $h_{\min} = 2 \times 10^{-6}$m and the maximum mesh size $h_{\max} = 1 \times 10^{-3}$m. The electron density is estimated to be $n_e \approx 10^{20}$ m^{-3}, so the refined mesh size h is set in as follows:

$$h = 1 \times 10^{-3} \times \frac{1}{2^9} \approx 1.95 \times 10^{-6}\text{m} < 2.0 \times 10^{-6}\text{m}. \tag{8}$$

The initial electron density is set to 10^5cm^{-3} uniformly distributed in the plasma region inside the quartz tube, and the initial ion density is distributed according to the quasi-neutral principle of plasma. The details of the boundary conditions for transport equations and Poisson equation are considered. The boundary conditions of the transport equations are shown in Table II. The boundary conditions for the Poisson equation include Dirichlet and Neumann. The former is a metal boundary $V = V(t)$, and the latter is $\nabla V = 0$. The Dirichlet boundary condition involves an accurate representation of the metal geometry, whereas the Cartesian mesh generates a jagged approximation on curved electrodes, which may affect the accurate representation of the electric potential. To solve this problem, the immersed boundary method is used.[26] The core idea of this approach is that the known metal boundary crosses two adjacent grids (inside and outside the metal, respectively). By using the known metal surface potential, the precise geometry, and the external metal potential, the potential of the internal metal grid can be obtained through linear interpolation.

C. The global model

For a long time scale, the 2D model is computationally expensive and time-consuming; therefore, the 0D global model is constructed to calculate the temporal evolution of species densities for detailed kinetics. A typical reaction in the plasma chemistry system can be described as follows:

$$aA + bB[+\delta\epsilon] \to a'A + cC[+\delta\epsilon], \tag{9}$$

$$R_j = k_j[A]^a[B]^b, \tag{10}$$

where A, B, and C are the species participating in the reaction, a, a', b, and c are the stochastic coefficients, R_j is the rate of reaction j, and k_j is the rate constant of reaction j. δ is the gradient of ϵ, and ϵ is the energy released (in right, product) or energy absorbed (in left, reactants) for the reaction. If the reactants are all heavy particles, the value of k_j can be considered as a function of the gas temperature; if Eq. (1) depicts an electron impact reaction, the value of k_j is a function of electron

TABLE II. Boundary conditions for transport equations.

Direction of flux	Electron	Electron energy	Negative ions	Positive ions
Input from anode	$\nabla n = 0$	$\Gamma_e = \Gamma_e n_e$	$\nabla n = 0$	0
Output from anode	0	0	0	$\nabla n = 0$
Input from cathode	0	0	0	$\nabla n = 0$
Output from cathode	$\nabla n = 0$	$\Gamma_e = \Gamma_e n_e$	$\nabla n = 0$	0
Input from dielectric	$\nabla \cdot \Gamma = 0$	$\Gamma_e = \Gamma_e n_e$	$\nabla \cdot \Gamma = 0$	$\nabla \cdot \Gamma = 0$
Output from dielectric	$\Gamma = -\gamma \cdot \Gamma_i$	$\Gamma_e = \Gamma_e \times 0.01$	0	0

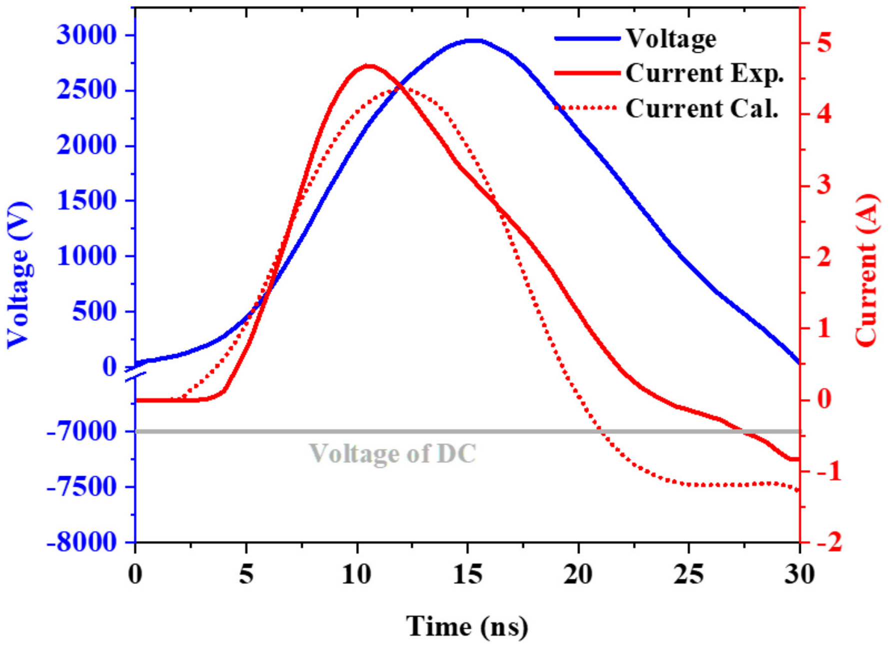

FIG. 4. Voltage waveforms of electrodes and comparison of the calculated current and the measured current.

temperature (T_e) or reduced electric field (E/N) calculated from the integration of the product of the electron impact cross section and electron energy distribution function (EEDF). The time evolution of the species of interest in the plasma chemistry system can be expressed as follows:

$$Q_A = (a' - a)R, \quad Q_B = -bR, \quad Q_C = cR, \tag{11}$$

$$\frac{d[N_i]}{dt} = \sum_{j=1}^{j_{max}} Q_{ij}(t), \tag{12}$$

where N_i is the i_{th} species in the system, j is the index of the reaction.

ZDPlasKin is an open Fortran code designed to apply the VODE solver[27] integral equations, and turn the chemotaxis into an initial value problem for solving ODEs. The code incorporates an inline two-term approximation Boltzmann equation solver (BOLSIG+) to calculate the EEDF and reaction rates at each time step. This solver has been widely acknowledged and validated by an increasing number of studies.[14] In this work, the reference solution of the plasma ODE system is solved using the ZDPlasKin code. The reaction kinetics mechanism used for air discharge simulations in this paper is based on the air plasma chemical reaction set, widely recognized and used by the plasma community, consisting of 55 species and 718 reactions. The kinetics mechanism contains electron, ion, neutral species and excited species: N_2, $N_2(v = 1 - 8)$, $N_2(a'^1\Sigma_u)$, $N_2(C^3\Pi_u)$, N, $N(^2D)$, $N(^2P)$, N^+, N_2^+, N_3^+, N_4^+, O_2, $O_2(v = 1 - 4)$, $O_2(a^1\Delta_g)$, $O_2(b^1\Sigma_g^+)$, $O_2(A^3\Sigma_u^+)$, $O_2(C^3\Delta_u)$, $O_2(c^1\Sigma_u^-)$, O, $O(^1D)$, $O(^1S)$, O_3, O^+, O_2^+, O_4^+, O^-, O_2^-, O_3^-, O_4^-, NO, NO^+, NO^-, $O_2^+N_2$, N_2O, NO_2, NO_3, N_2O_5, $N_2O_2^+$, NO_2^-, NO_3^-. The kinetics mechanism has been repeatedly tested both experimentally and computationally.[28] Additionally, the rate constant of reactions in nitrogen–oxygen mixtures are listed in Refs. 24 and 29. The reduced electric field $E/N(t)$, as the input parameters of the global model, is critical for characterizing the pulse discharge. The 2D model provided $E/N(t)$ and the initial species densities to the 0D model to calculate the temporal evolution of species densities. The $E/N(t)$ and initial species densities are extracted from the fixed position in the 2D model after achievement of the discharge channel.

III. RESULTS AND DISCUSSION

A. The base case

In this study, since the discharge mechanism cannot be explained by the experiment, a two-dimensional fluid model is used to analyze the behavior of a three-electrode discharge in air at atmospheric pressure. The general scheme of the experimental setup is shown in Fig. 1, where nanosecond pulses with a voltage amplitude of 3 kV and a rising edge of 10 ns are applied to the HV electrode. The experimentally measured voltage serves as a key input parameter for the fluid model. As shown in Fig. 4, two voltage probes simultaneously monitor the waveforms of the DBD and DC electrodes. The DC electrode measurement reveals a constant voltage rather than an oscillating waveform. In addition, Fig. 4 demonstrates that the calculated current shows good agreement with the experimental measurements. Figure 5 presents the temporal and spatial discharge evolution captured by ICCD and the simulated $N_2(C^3\Pi_u)$ density distribution, both of which show good agreement. In Fig. 5(a), the surface streamer originates near the triple point at the high-voltage electrode edge and propagates along the dielectric surface. Due to the enhanced electric field at its ionization front, the surface streamer propagates significantly faster than its volumetric counterpart. The discharge initiates as a set of highly synchronized streamers from the electrode edge.

Figure 6 presents temporal and spatial evolution of electron density and E/N, revealing that discharge can be divided into three processes. During the initial 20 ns period, the positive pulse DBD and the negative DC discharge operate independently. For positive polarity, the electron density of DBD remains relatively uniform across the channel while exhibiting a temporal decay throughout the structure.

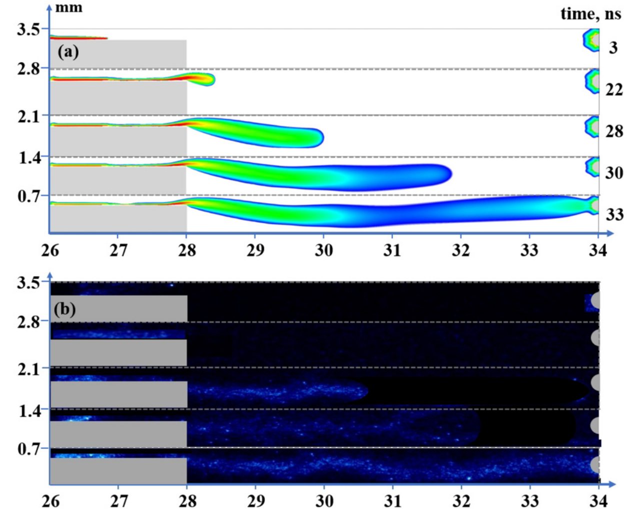

FIG. 5. Comparison of the calculated and experiment $N_2(C^3\Pi_u)$ by ICCD imaging technique. (a) Evolution of discharge calculated by fluid model. (b) Evolution of discharge measured by ICCD.

Between 20 and 30 ns, the discharge transitions to a space discharge regime, exhibiting distinct charge separation at the streamer head and enhanced plasma propagation velocity. This transition initiates with primary electron avalanches, where field-accelerated electrons ionize surrounding gas molecules. The resulting space charge distortion from slower positive ions locally enhances the electric field, triggering secondary ionization through photon-mediated processes ahead of the advancing front. From 30 to 33 ns, when DC discharge-induced pre-ionization density exceeds a critical threshold (2×10^{17} m^{-3}), resulting in overlapping spatial electrons. This effect smooths the electric field gradient,[30] facilitating a transition from streamer to diffuse discharge.

In order to further analyze the discharge mechanism, the distributions of electron density and E/N along the $y = 23.02$ mm line are extracted, as shown in Fig. 7. Three distinct discharge regimes are identified along the propagation path: (1) In the surface discharge regime ($x = 26$–28 mm), the discharge remains attached to the dielectric surface, with the DBD streamer thickness well characterized by the analytical model of Soloviev *et al.*[25] This region exhibits typical surface streamer characteristics with strong field enhancement at the ionization front. (2) In the transition region to space discharge ($x = 28$–29.5 mm), the discharge detaches from the surface, evolving

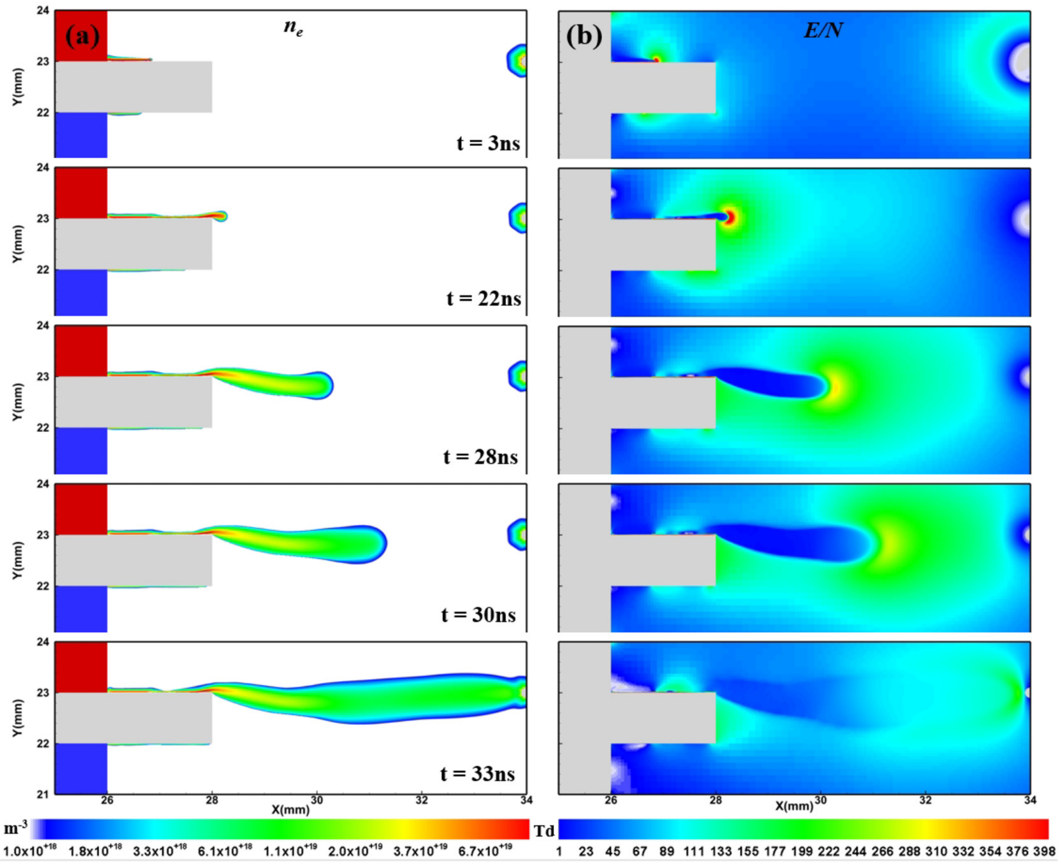

FIG. 6. Temporal and spatial evolution of three-electrode discharge. (a) Electron density in units of m^{-3}. (b) Reduced electric field in units of Td.

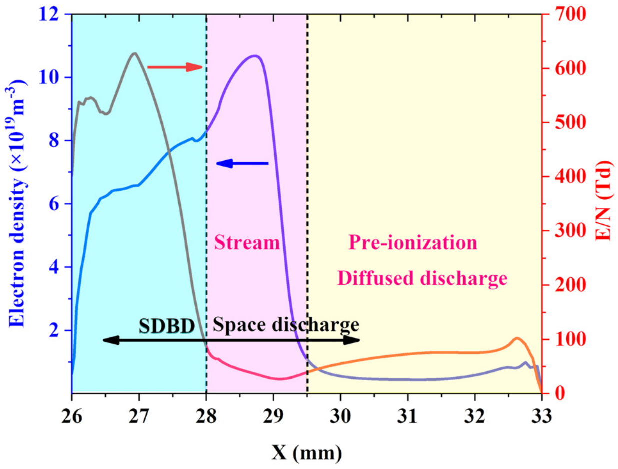

FIG. 7. Distribution of electron density and E/N along the $y = 23.02$ mm line.

into a volumetric streamer channel. The absence of charge accumulation in this region leads to progressive field attenuation as the interelectrode distance increases, resulting in a significant decrease in electron density. (3) In the diffuse discharge ($x = 29.5$–34 mm) region generally, pre-ionization is required to develop a diffuse volume discharge, and sufficient pre-ionization suppresses the formation of filamentary streamer and prevents their transition into spark.[31] As the spatial discharge propagates to the needle electrode, DC discharge-induced pre-ionization enables the discharge mode transition from spatial to diffuse. The emission of electrons, which attach to oxygen molecules to form negative ions, occurs from a negative conductor. The boundary of negative ions forms an approximately cylindrical distribution surrounding the high-voltage needle, with the ion cloud extending radially along the needle's length. Because of the presence of the DBD setup near the needle, the negative ion distribution undergoes distortion—shifting leftward from original cylindrical shape, and merges with the ion cloud of space discharge to bridge the gas gap. This spatial negative ion distribution modifies the local electric field profile, facilitating the observed discharge mode transition.

B. Effect of DC electrode on discharge

In this study, the effects of DC electrode diameter and location on discharge was analyzed under consistent voltage parameters ($V_p = 4$ kV, $V_{DC} = 7$ kV) and a fixed discharge gap ($d = 8$ mm). Figure 8 illustrates the distribution of electron density and E/N for four different electrode diameters. It is observed that the breakdown time for four cases is the same. Smaller diameters generate a stronger electric field, resulting in a larger plasma area near the DC electrode. To further investigate the discharge mechanism, the spatial distribution of E/N along $y = 23.02$ mm is shown in Fig. 8. As the diameter increases, the peak E/N drops from 640 to 575 Td, while the streamer propagation velocity remains unchanged. Despite the reduction in peak E/N, the diameter increase also reduces the discharge gap, maintaining the time of the discharge channel formation. In the stream propagation stage, the electron density decreases with increase in electrode diameter, while in the diffuse discharge stage, the electron density is basically the same. Near the DC electrode, the density also decreases with increase in electrode diameter due to the different strength of DC discharge.

The selection of electrode diameters in practical applications requires careful consideration of deformation resistance and processing costs, as these factors critically influence discharge performance and system reliability. When the diameter becomes excessively small (typically below 0.5 mm), the enhanced electric field concentration at the sharper tip leads to stronger but more unstable discharge characteristics. However, this advantage comes with significant drawbacks, including substantially higher manufacturing costs and greater susceptibility to thermal damage, particularly electrode burning and tip deformation under high-current operation. Conversely, bigger electrodes demonstrate compromised discharge efficiency due to reduced field intensity, resulting in poor chemical activity. This performance degradation often necessitates higher power input to maintain desired discharge characteristics while potentially introducing plasma confinement challenges in constrained geometries. For most atmospheric pressure plasma applications, an intermediate diameter range of 0.6–0.8 mm represents an optimal balance between electrical performance and mechanical reliability.

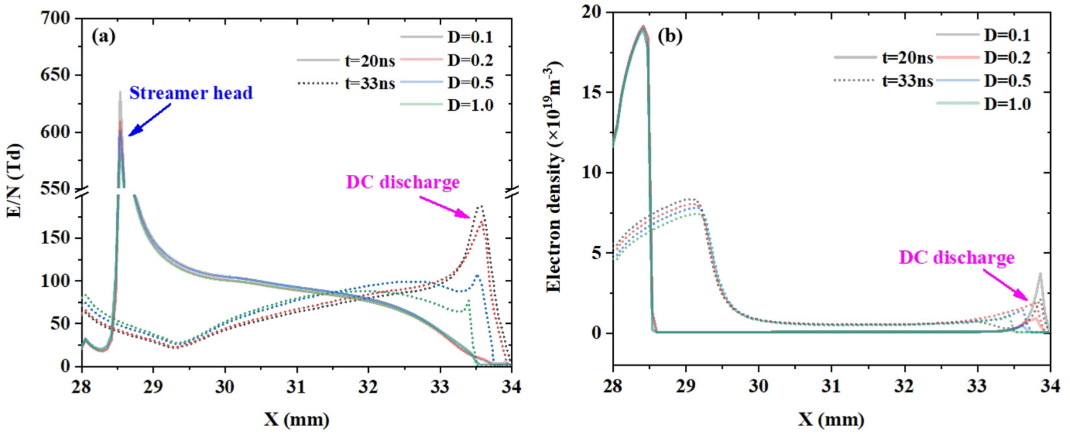

FIG. 8. Distribution of E/N and electron density at different DC electrode diameter and time. (a) Reduced electric field in units of Td. (b) Electron density in units of m^{-3}.

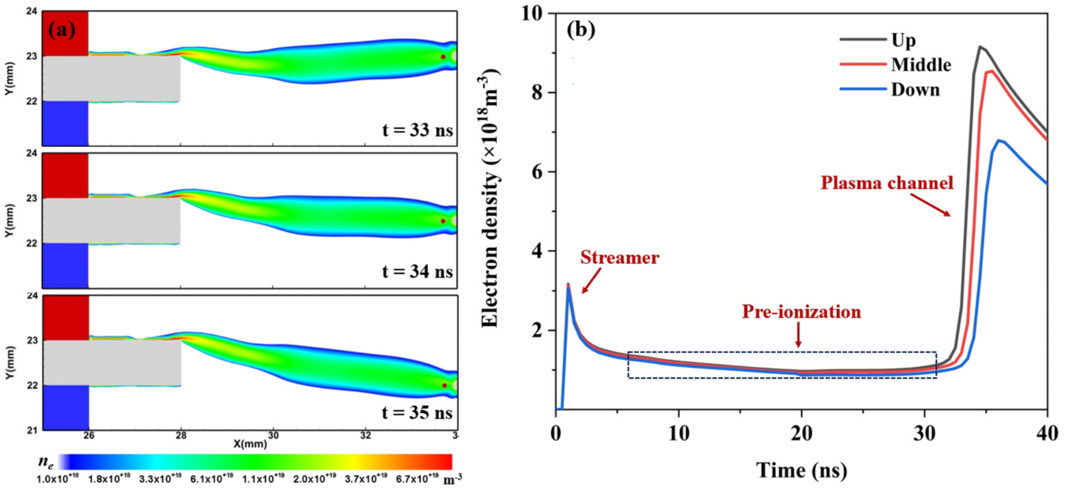

FIG. 9. Spatial distribution and temporal evolution of electron density at various DC electrode positions. (a) Spatial distribution of electron density at the breakdown time. (b) Temporal evolution of electron density of three points in (a).

The effect of DC electrode location on discharge was analyzed using the same voltage parameters ($V_p = 4$ kV, $V_{DC} = -7$ kV) and DC electrode diameter ($D = 0.1$ mm). The distributions of electron density at three different locations are shown in Fig. 9. It is observed that the breakdown time varies at the three different locations. The shortest breakdown time is observed in the region closest to the DC electrode, where the electric field is intensified by the reduced distance between the electrodes. The electron density distribution at the breakdown time reveals that the spatial discharge propagates from the upper surface of the SDBD to the DC electrode, while no propagation is observed from the middle or lower surfaces. The plasma coverage area remains essentially unchanged. In addition, the temporal evolution of electron density is analyzed at a fixed position to the right of the DC electrode. An initial peak in electron density is observed as the head of the DC discharge stream reaches this point, followed by the maintenance of a pre-ionization state once the stream passes. During this phase, the electron density stabilizes around $10^{18}\mathrm{m}^{-3}$. A sharp rise in electron density occurs as the DBD streamer traverses the pre-ionization region. Subsequently, as the electric field becomes uniform with the formation of the discharge channel, the electron density decreases.

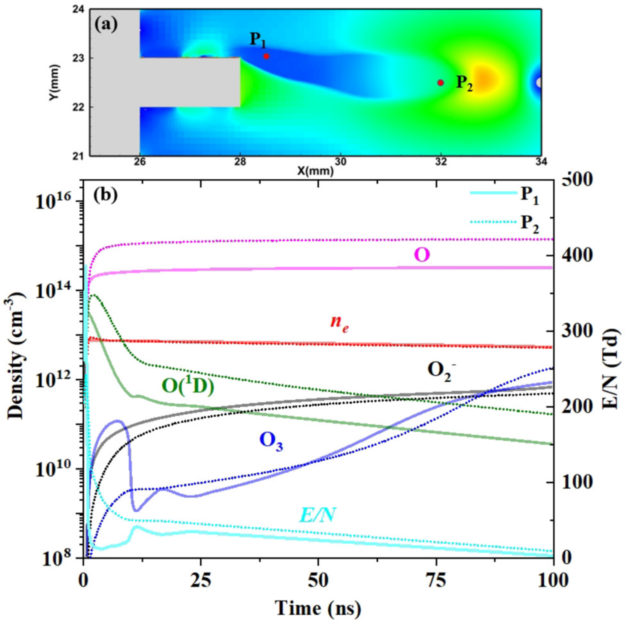

FIG. 10. Temporal evolution of active species densities. (a) Spatial distribution of E/N at the breakdown time. (b) Temporal evolution of active species densities at two points in (a).

The two-point electric field of the spatial discharge is extracted and used as input for the 0D model to analyze the reaction dynamics. A large number of active particles, including electrons, excited species, ions, and free radicals, play a crucial role in the gas treatment. The results of the zero-dimensional reaction kinetics calculations are presented in Fig. 10. The spatial distribution of the electric field is relatively uniform, leading to a consistent temporal evolution of component densities. However, slight differences in species densities are observed, with higher concentrations near the DC electrode region.

C. The analysis of breakdown voltage

The breakdown voltage of SDBD can be calculated using the following analytical equation derived from Ref. 32:

$$V_{bd} \approx \frac{\pi B(1+\alpha_\varepsilon)}{2k_\varepsilon}\sqrt{\frac{pd\ln\left(1+\gamma^{-1}\right)}{A}}, \tag{13}$$

where A and B are the fitting parameters of the Townsend ionization, $A = 15\,\mathrm{cm}^{-1}\mathrm{Torr}^{-1}$, $B = 365\,\mathrm{V cm}^{-1}\mathrm{Torr}^{-1}$ in the air. ε is the relative dielectric constant of the material, and k_ε is the fitting parameter of ε (when $\varepsilon = 3$–10, $k_\varepsilon = 1.2$). $\gamma_s = 0.01$ is the second electron emission coefficient of cathode. Therefore, under atmospheric pressure air

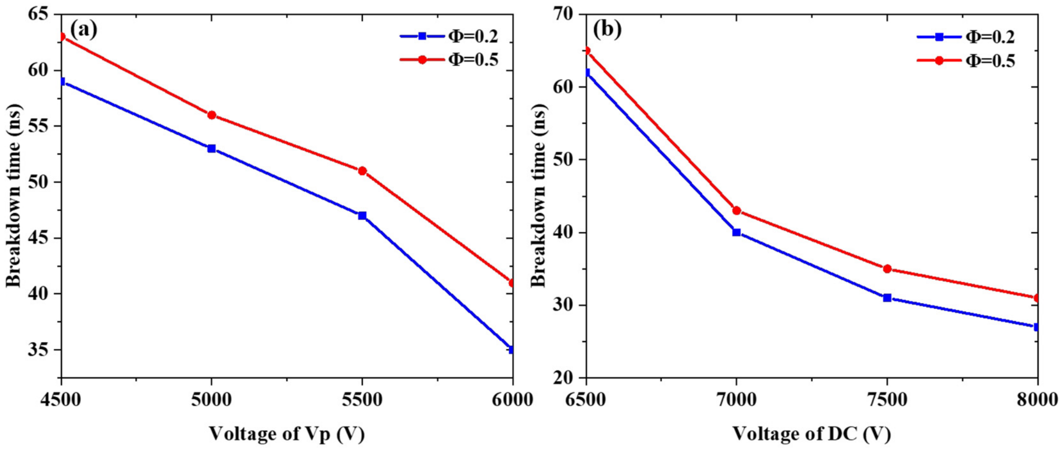

FIG. 11. Breakdown voltage and time at different DC electrode diameters. (a) Variation of breakdown time with the peak voltage of DBD at the $V_{DC} = -6000$ V. (b) Variation of breakdown time with DC voltage at the $V_p = 3500$ V.

SDBD discharge conditions, the breakdown voltage is 2.4 kV when the relative dielectric constant is set to 9.

Based on the experimental results, a minimum DC voltage of −6 kV and a minimum pulse voltage of 3.5 kV are required for breakdown, indicating that the traditional breakdown voltage formula for SDBD is no longer applicable to this structure. For this configuration, it is necessary not only to meet the SDBD breakdown voltage but also to ensure that the discharge propagation distance is sufficient to form a spatial discharge with the DC electrode, thereby bridging the entire discharge gap.

To further investigate the breakdown voltage for different electrode diameters ($D = 0.2$ mm and $D = 0.5$ mm), a discharge gap of $d = 8$ mm was selected. To isolate the effect of a single variable, the discharge characteristics of DBD were calculated for peak voltages of $V_{DC} = -6$ kV and $V_p = 3.5$ kV, respectively. The calculated breakdown voltage and time results are shown in Fig. 11. The analysis indicates that the entire discharge channel is only established when V_p exceeds 3.5 kV, with the breakdown time decreasing as V_p increases. Additionally, a comparison between the two DC electrode diameters reveals that the breakdown time is shorter for a smaller diameter, suggesting that the DC electrode diameter is a crucial parameter affecting discharge. When V_p is fixed at 3.5 kV, increasing V_{DC} significantly reduces the breakdown time for both electrode diameters. In terms of discharge power for this structure, the majority of power consumption is attributed to DBD. Therefore, in practical applications, it is advisable to keep V_p as low as possible to minimize total power consumption.

IV. CONCLUSION

This study investigates the dynamics and optimization of a three-electrode discharge system, combining DBD and DC discharge, to address challenges in low-temperature plasma applications for gas treatment and energy conversion. The research focuses on enhancing discharge stability and efficiency by analyzing the effects of electrode structure and discharge parameters.

Through experiments and two-dimensional fluid simulations, the study identifies key factors influencing the transition from streamer to diffuse discharge in atmospheric pressure air. Results reveal that pre-ionization induced by the DC discharge plays a critical role, requiring a minimum density of $2 \times 10^{17}\,\mathrm{m}^{-3}$ to achieve this transition. During this process, the discharge evolves from a streamer mode to a spatial discharge, with pre-ionization smoothing the electric field gradient and enabling the formation of a stable discharge channel.

The study further highlights the impact of electrode diameter and location on discharge characteristics. Smaller DC electrode diameters generate stronger electric fields and higher plasma densities near the electrode, while larger diameters reduce peak E/N but maintain discharge due to shorter discharge gaps. Additionally, a minimum DC voltage of −6 kV and a DBD voltage of 3.5 kV are required to form a complete discharge channel, with breakdown times decreasing as V_p and V_{DC} increase. Most power consumption is attributed to the DBD, suggesting that minimizing V_p is key to reducing total power in practical applications.

This work provides valuable insights into achieving stable and energy-efficient plasma discharges. It establishes the critical role of electrode structure and discharge parameters in optimizing performance, addressing challenges such as small area discharge and limited active species generation. These findings pave the way for scalable plasma technologies in gas treatment, offering improved stability and efficiency. Future research should focus on further enhancing plasma source performance, understanding active species dynamics, and adapting the system for complex engineering environments.

ACKNOWLEDGMENTS

The work is supported by the National Natural Science Foundation Basic Science Center Project (52488101), the National Key Research and Development Program of China (2022YFC2604002), and the National Natural Science Foundation of China (Nos. 52277168, 52025064, and 92271113). The authors thank the young research group in Atelier des Plasmas for fruitful discussions and the Gongfang Tech Co, Ltd for technical support.

AUTHOR DECLARATIONS

Conflict of Interest

The authors have no conflicts to disclose.

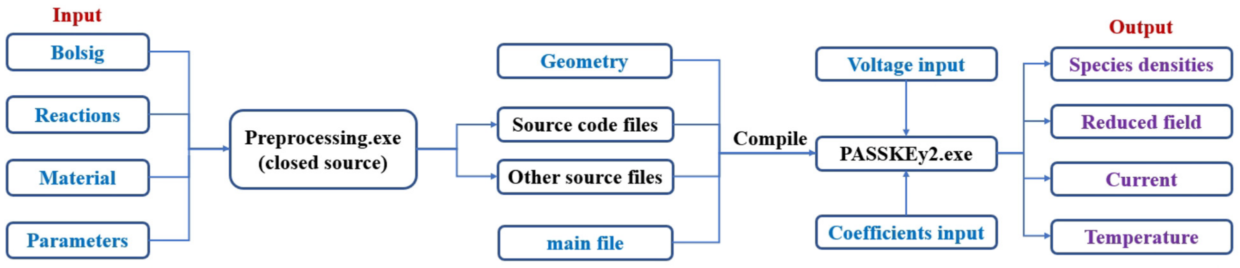

FIG. 12. Details on the PASSKEY model's input and output data specifications. Colors are used to distinguish components: blue (input), purple (output), and black (runtime process).

Author Contributions

Bo YIN: Data curation (equal); Writing – original draft (equal); Writing – review & editing (equal). **Xiaochi MA:** Data curation (equal); Methodology (equal); Validation (equal). **Yifei ZHU:** Methodology (equal); Supervision (equal); Writing – original draft (equal). **Yun Wu:** Supervision (equal). **Borui Zheng:** Conceptualization (equal); Formal analysis (equal).

DATA AVAILABILITY

The data that supports the findings of this study are available within the article.

APPENDIX: DETAILS ON PASSKEY MODEL

The 2D PASSKEy code is used to calculate spatial-temporal evolution of the electric field, species densities, and fluid dynamics in non-thermal plasmas with complex chemistry. Details of the model's input and output are shown in Fig. 12. Detailed mathematical methods and model validations can be found in Sec. II. A Boltzmann equation solver (BOLSIG+) incorporated in PASSKEy model provides values of electron transport and rate coefficients when the electron energy distribution function is non-Maxwellian. PASSKEy operates in three steps:

Step I: The preprocessor converts the input files (Bolsig, reactions, material, and parameters) into two customized Fortran modules.
Step II: The user implements a short master code (main file) to call Fortran modules and geometry file, compiling into an executable file (PASSKEy2.exe).
Step III: The executable file reads the voltage input and coefficients input to generate the results (species densities, E/N, current, and temperature).

REFERENCES

[1] S. Li, X. Dang, X. Yu, G. Abbas, Q. Zhang, and L. Cao, "The application of dielectric barrier discharge non-thermal plasma in VOCs abatement: A review," Chem. Eng. J. **388**, 124275 (2020).

[2] X. Gong, Y. Lin, X. Li, A. Wu, H. Zhang, J. Yan, and C. Du, "Decomposition of volatile organic compounds using gliding arc discharge plasma," J. Air Waste Manage. Assoc. **70**(2), 138–157 (2020).

[3] H. Zeghioud, P. Nguyen-Tri, L. Khezami, A. Amrane, and A. A. Assadi, "Review on discharge plasma for water treatment: Mechanism, reactor geometries, active species and combined processes," J. Water Process Eng. **38**, 101664 (2020).

[4] K. Kučerová, Z. Machala, and K. Hensel, "Transient spark discharge generated in various N_2/O_2 gas mixtures: Reactive species in the gas and water and their antibacterial effects," Plasma Chem. Plasma Process. **40**, 749–773 (2020).

[5] M. Gundersen, P. T. Vernier, S. B. Cronin, and S. Kerketta, "A review of diverse academic research in nanosecond pulsed power and plasma science," IEEE Trans. Plasma Sci. **48**(4), 742–748 (2020).

[6] C. Dobslaw and B. Glocker, "Plasma technology and its relevance in waste air and waste gas treatment," Sustainability **12**(21), 8981 (2020).

[7] S. Stepanyan, V. Soloviev, and S. Starikovskaia, "An electric field in nanosecond surface dielectric barrier discharge at different polarities of the high voltage pulse: Spectroscopy measurements and numerical modeling," J. Phys. D: Appl. Phys. **47**(48), 485201 (2014).

[8] S. Tao, L. Kaihua, Z. Cheng, Y. Ping, Z. Shichang, and P. Ruzheng, "Experimental study on repetitive unipolar nanosecond-pulse dielectric barrier discharge in air at atmospheric pressure," J. Phys. D: Appl. Phys. **41**(21), 215203 (2008).

[9] C. Liu, A. Fridman, and D. Dobrynin, "Uniformity analysis of nanosecond and sub-nanosecond pulsed DBD in atmospheric air," Plasma Res. Express **1**(1), 015007 (2018).

[10] A. Belinger, S. Dap, and N. Naudé, "Influence of the dielectric thickness on the homogeneity of a diffuse dielectric barrier discharge in air," J. Phys. D: Appl. Phys. **55**(46), 465201 (2022).

[11] Y. Zhu, Y. Wu, B. Wei, H. Xu, H. Liang, M. Jia, H. Song, and Y. Li, "Nanosecond-pulsed dielectric barrier discharge-based plasma-assisted anti-icing: Modeling and mechanism analysis," J. Phys. D: Appl. Phys. **53**(14), 145205 (2020).

[12] Y. Zhu and S. Starikovskaia, "Fast gas heating of nanosecond pulsed surface dielectric barrier discharge: Spatial distribution and fractional contribution from kinetics," Plasma Sources Sci. Technol. **27**(12), 124007 (2018).

[13] X. Ma, L. Bai, Y. Zhu, X. Jiang, and Y. Wu, "Numerical investigation of discharge evolution and breakdown characteristics of ArF excimer lasers," Plasma Sources Sci. Technol. **33**(7), 075012 (2024).

[14] G. Hagelaar and L. C. Pitchford, "Solving the Boltzmann equation to obtain electron transport coefficients and rate coefficients for fluid models," Plasma Sources Sci. Technol. **14**(4), 722 (2005).

[15] L. Viehland and E. Mason, "Transport properties of gaseous ions over a wide energy range, IV," At. Data Nucl. Data Tables **60**(1), 37–95 (1995).

[16] B. Bagheri, J. Teunissen, U. Ebert, M. M. Becker, S. Chen, O. Ducasse, O. Eichwald, D. Loffhagen, A. Luque, D. Mihailova *et al.*, "Comparison of six simulation codes for positive streamers in air," Plasma Sources Sci. Technol. **27**(9), 095002 (2018).

[17] P. Viegas, E. Slikboer, Z. Bonaventura, O. Guaitella, A. Sobota, and A. Bourdon, "Physics of plasma jets and interaction with surfaces: Review on modelling and experiments," Plasma Sources Sci. Technol. **31**(5), 053001 (2022).

[18] G. Grubert, M. Becker, and D. Loffhagen, "Why the local-mean-energy approximation should be used in hydrodynamic plasma descriptions instead of the local-field approximation," Phys. Rev. E **80**(3), 036405 (2009).

[19] A. Phelps and L. Pitchford, "Anisotropic scattering of electrons by N_2 and its effect on electron transport," Phys. Rev. A **31**(5), 2932 (1985).

[20] S. Lawton and A. Phelps, "Excitation of the $b\ ^1\sum_g^+$ state of O_2 by low energy electrons," J. Chem. Phys. **69**(3), 1055–1068 (1978).

[21] I. Kossyi, A. Y. Kostinsky, A. Matveyev, and V. Silakov, "Kinetic scheme of the non-equilibrium discharge in nitrogen-oxygen mixtures," Plasma Sources Sci. Technol. **1**(3), 207 (1992).

[22] N. Popov, "Fast gas heating in a nitrogen–oxygen discharge plasma: I. Kinetic mechanism," J. Phys. D: Appl. Phys. **44**(28), 285201 (2011).

[23] S. Pancheshnyi, M. Nudnova, and A. Starikovskii, "Development of a cathode-directed streamer discharge in air at different pressures: Experiment and comparison with direct numerical simulation," Phys. Rev. E **71**(1), 016407 (2005).

[24] M. Capitelli, C. M. Ferreira, B. F. Gordiets, and A. I. Osipov, *Plasma Kinetics in Atmospheric Gases* (Springer Science & Business Media, 2013), Vol. 31.

[25] V. R. Soloviev and V. M. Krivtsov, "Numerical modelling of nanosecond surface dielectric barrier discharge evolution in atmospheric air," Plasma Sources Sci. Technol. **27**(11), 114001 (2018).

[26] S. Celestin, Z. Bonaventura, B. Zeghondy, A. Bourdon, and P. Ségur, "The use of the ghost fluid method for Poisson's equation to simulate streamer propagation in point-to-plane and point-to-point geometries," J. Phys. D: Appl. Phys. **42**(6), 065203 (2009).

[27] P. N. Brown, G. D. Byrne, and A. C. Hindmarsh, "VODE: A variable-coefficient ODE solver," SIAM J. Sci. Stat. Comput. **10**(5), 1038–1051 (1989).

[28] B. Yin, Y. Zhu, and Y. Wu, "Modulating sparks in a pulse train for repetitive and energy efficient plasma generation," High Voltage **8**(6), 1168–1179 (2023).

[29] Y. Zhu, N. D. Lepikhin, I. S. Orel, A. Salmon, A. V. Klochko, and S. M. Starikovskaia, "Optical actinometry of O-atoms in pulsed nanosecond capillary discharge: Peculiarities of kinetics at high specific deposited energy," Plasma Sources Sci. Technol. **27**(7), 075020 (2018).

[30] J. I. Levatter and S.-C. Lin, "Necessary conditions for the homogeneous formation of pulsed avalanche discharges at high gas pressures," J. Appl. Phys. **51**(1), 210–222 (1980).

[31] T. Shao, V. F. Tarasenko, C. Zhang, E. K. Baksht, P. Yan, and Y. V. Shut'Ko, "Repetitive nanosecond-pulse discharge in a highly nonuniform electric field in atmospheric air: X-ray emission and runaway electron generation," Laser Part. Beams **30**(3), 369–378 (2012).

[32] V. Soloviev, I. Selivonin, and I. Moralev, "Breakdown voltage for surface dielectric barrier discharge ignition in atmospheric air," Phys. Plasmas **24**(10), 103528 (2017).